Article:
Olivieri, DA, Fairweather, M and Falle, SAEG (2011) Prediction of external intermittency using RANS-based turbulence modelling and a transported PDF approach. Computers and Fluids, 47 (1). 75 - 84. ISSN: 0045-7930

https://doi.org/10.1016/j.compfluid.2011.02.017

Prediction of External Intermittency Using RANS-Based Turbulence Modelling and a Transported PDF Approach

D.A. Olivieri[a,*], M. Fairweather[a], S.A.E.G. Falle[b]
[a]*School of Process, Environmental and Materials Engineering, The University of Leeds, Leeds LS2 9JT,UK*
[b]*School of Mathematics, The University of Leeds, Leeds LS2 9JT, UK*

Abstract
This paper investigates the modelling of external intermittency in turbulent round jets using a RANS approach coupled to solutions of the transported probability density function (PDF) equation for scalar variables. Solutions to the descriptive equations are obtained using a finite-volume method, combined with an adaptive mesh refinement algorithm, applied in both physical and compositional space. The effects of intermittency on the flow field are accommodated using intermittency-modified eddy viscosity and second-moment turbulence closures, as well as through modifications to the mixing model embodied within the transported PDF equation. Predictions of the model are validated against data on the velocity and scalar fields in jets, as well as against measurements of scalar PDFs and intermittency profiles, with reasonable agreement obtained. From the cases examined, predictions of the second-moment closure are superior, although both approaches provide realistic predictions of the bimodal features to the measured PDFs.

Keywords: Intermittency; Reynolds-averaged Navier-Stokes; transported PDF; finite-volume method; adaptive mesh refinement

---

1. Introduction

Turbulent shear flows with free boundaries display an intermittent character where the flow rapidly alternates between rotational and irrotational states. Such intermittency is frequently referred to as external intermittency to distinguish it from the internal form which concerns the variability of the energy or scalar dissipation rates. External intermittency can be thought of as an indicator function that has a value of unity when the flow is turbulent and zero when it is non-turbulent, i.e. it represents the fraction of time during which a point is inside the turbulent fluid.

Intermittency is important in many practical flows. For example, the ignition of turbulent flows of flammable material, and the safe and efficient operation of many combustion devices, is critically dependent on ignition occurring in flows which contain significant intermittency, and the enhanced performance

[*]Corresponding author. Tel.: +44 113 343 2419; fax.: +44 113 343 2405
Email address: d.a.olivieri@leeds.ac.uk (D.A. Olivieri)

of these devices and improved safety relies on a detailed understanding of the flow and ignition processes. More broadly, the intermittent behaviour of flows is also influential in other generic processes, including mixing, combustion, emissions and aero-acoustics.

The majorities of turbulence models currently in use were derived for fully developed flows, and hence cannot be expected to predict accurately in free shear flows where the outer regions contain irrotational flow. The development of more accurate engineering models of turbulence that accommodate intermittency effects is therefore of fundamental importance. Intensive research efforts have also been devoted to developing more general engineering turbulence models in recent years, although their predictability generally remains dependent on flow configuration. Improvements in the both the accuracy and generality of these models can, however, be made through the incorporation of intermittency effects. An important example of this is seen in the round jet/plane jet anomaly [1], where the inclusion of intermittency effects within a conventional k-ε turbulence model has been demonstrated [2] to resolve this discrepancy. In general terms, therefore, the provision of reliable intermittency-based turbulence models will not only permit the more accurate prediction of the velocity and scalar fields of interest in the applications noted above, but should result in more generally applicable models that are less dependent on flow configuration.

This paper describes an investigation into the modelling of intermittency in turbulent flows using solutions of the transported probability density function (PDF) equation for scalar variables obtained using a finite-volume method combined with an adaptive mesh refinement (AMR) algorithm. The effects of intermittency on the turbulent flow field have been accommodated in a conventional Reynolds-averaged Navier-Stokes (RANS) modelling framework using intermittency-corrected eddy viscosity and second-moment turbulence closures, with the influence of intermittency on the PDF included via the mixing model embodied within its transport equation. This contrasts to the earlier approach of Kollmann and co-workers [3–6] which used a finite-difference approach to solving the PDF transport equation coupled to a closure scheme based on conditional zone-averaged moments, rather than the Reynolds-averaged moments used in the present work. Predictions of the complete model are validated against experimental data available in the literature on the velocity and scalar fields in turbulent round jets, as well as against measurements of scalar PDFs and intermittency profiles.

Earlier work by the authors [7, 8] has demonstrated the application of an AMR finite-volume technique in both physical and compositional space, with the latter permitting solution of the transported PDF equation. This contrasts with more conventional approaches which are based on the use of finite-volume methods in physical space, and Monte Carlo methods in compositional space for solution of the PDF equation. This work [7, 8] also demonstrated that, for small numbers of scalar variables, AMR provides improved accuracy, run times and ease of use over alternative Monte Carlo approaches. AMR is now a well-established technique, having its earliest applications in two-dimensional shock problems [9, 10], with subsequent extension to three-dimensional flows [11] and implementation on parallel computers [12]. The advantage of AMR over uniform mesh approaches is that it uses error estimates to adaptively increase grid resolution to meet accuracy

requirements in specific parts of the computational domain, whilst de-refining in regions where few changes are taking place. In some classes of problems, CPU and memory requirements can be reduced over those for a uniform grid by as much as a factor of one hundred [13]. As noted, the present work extends these earlier applications of AMR by employing the approach in both physical and compositional space in order to predict the intermittent flows of interest.

2. Mathematical modelling

2.1. Fluid flow equations closed using k-ε-γ model

The flow was computed using the mass and momentum conversation equations for turbulent flow in cylindrical symmetry, closed using a *k-ε-*γ turbulence model [2], together with the thin shear layer and parabolic approximations for steady flow [14]. It was assumed that the turbulence was statistically two-dimensional, stationary and non-swirling. The flow equations are then given, in density-weighted form, as:

$$
\begin{aligned}
&\frac{\partial(\rho\tilde{u})}{\partial z}+\frac{1}{r}\frac{\partial(r\rho\tilde{v})}{\partial r}=0,\\
&\rho\tilde{u}\frac{\partial\tilde{u}}{\partial z}+\rho\tilde{v}\frac{\partial\tilde{u}}{\partial r}=\frac{1}{r}\frac{\partial}{\partial r}r\mu\frac{\partial\tilde{u}}{\partial r},\\
&\rho\tilde{u}\frac{\partial k}{\partial z}+\rho\tilde{v}\frac{\partial k}{\partial r}=\frac{1}{r}\frac{\partial}{\partial r}r\frac{\mu}{\sigma_k}\frac{\partial k}{\partial r}+\mu\left(\frac{\partial\tilde{u}}{\partial r}\right)^2-\rho\varepsilon,\\
&\rho\tilde{u}\frac{\partial\varepsilon}{\partial z}+\rho\tilde{v}\frac{\partial\varepsilon}{\partial r}=\frac{1}{r}\frac{\partial}{\partial r}r\frac{\mu}{\sigma_\varepsilon}\frac{\partial\varepsilon}{\partial r}+\frac{\varepsilon}{k}\left[C_{\varepsilon1}\mu\left(\frac{\partial\tilde{u}}{\partial r}\right)^2-C_{\varepsilon2}\rho\varepsilon+\rho\varepsilon C_{\varepsilon4}\Gamma\right],\\
&\rho\tilde{u}\frac{\partial\gamma}{\partial z}+\rho\tilde{v}\frac{\partial\gamma}{\partial r}=\frac{1}{r}\frac{\partial}{\partial r}r\frac{\mu(1-\gamma)}{\sigma_\gamma}\frac{\partial\gamma}{\partial r}+\frac{\mu\gamma(1-\gamma)C_{\gamma1}}{k}\left(\frac{\partial\tilde{u}}{\partial r}\right)^2\\
&\qquad+C_{\gamma2}\rho\frac{k^2}{\varepsilon}\left(\frac{\partial\gamma}{\partial r}\right)^2-C_{\gamma3}\gamma(1-\gamma)\frac{\rho\varepsilon}{k}\Gamma
\end{aligned}
\tag{1}
$$

Here $\tilde{u}$ and $\tilde{v}$ are the mean velocities in the *z* and *r* directions, respectively, and σ_k, σ_ε and σ_γ are the Prandtl numbers for *k*, *ε* and γ. Due to the thin shear layer approximation, only the *u*-component of the momentum equation is employed. The turbulent viscosity *μ* and Galilean invariance Γ are given as follows:

$$
\begin{aligned}
\mu &= C_\mu\rho\frac{k^2}{\varepsilon}\left[1+\frac{k^3}{\varepsilon^2}C_{\mu\gamma}\gamma^3(1-\gamma)\left(\frac{\partial\gamma}{\partial r}\right)^2\right],\\
\Gamma &\equiv \frac{k^{5/2}}{\varepsilon^2}(\nabla|U|)\cdot(\nabla\gamma)=\frac{k^{5/2}}{\varepsilon^2}\left(\frac{\tilde{u}}{\sqrt{\tilde{u}^2}}\frac{\partial\tilde{u}}{\partial r}\frac{\partial\gamma}{\partial r}\right)
\end{aligned}
\tag{2}
$$

where *U* is the total flow velocity vector. Note that for the thin shear layer approximation $|U|\cong\tilde{u}$. The final expression in (1) provides a transport equation for γ itself. The first term on the right hand side of this equation describes the bulk convective spatial transport due to turbulent flow, whilst the other terms on the right hand side contribute to the source term which

describes the mean rate of entrainment of non-turbulent fluid into the turbulent zone. The source term of this equation represents the main part of the Cho and Chung [2] model.

The Galilean invariance used in modifying the source term of the turbulence energy dissipation rate equation represents the amount of intermittency entrained by the interaction between the mean velocity gradient and the intermittency, per unit volume of the flow field. When the flow intermittency is small, small-scale eddies are relatively inactive and the turbulence kinetic energy is dissipated slowly. If intermittency is large, then small eddies become embedded in the large straining eddies in the interactive shear layer between the turbulent and irrotational zones. The Γ parameter therefore indicates how much of a source or sink of dissipation is occurring due the entrainment of more-irrotational fluid at a particular point.

It is assumed that the pressure is constant, which avoids the need for a Poisson equation solver. As will be seen below, this is a reasonable approximation for the jet flows examined. The continuity equation is unnecessary since the density can be calculated from the average mass fractions $<\omega_\alpha>$:

$$\frac{1}{\rho} = \sum_{\alpha=1}^{N} \frac{<\omega_\alpha>}{\rho_\alpha}, \tag{3}$$

where ρ_α is the density of a fluid with an average mass fraction $<\omega_\alpha> = 1$.

Standard modelling constants [15] were used in conjunction with the k-ε-γ approach, with $C_\mu = 0.09$, $C_{\mu\gamma} = 0.1$, $C_{\varepsilon 1} = 1.44$, $C_{\varepsilon 2} = 1.92$, $C_{\varepsilon 4} = 0.1$, $C_{\gamma 1} = 1.6$, $C_{\gamma 2} = 0.15$, $C_{\gamma 3} = 0.16$, $C_D = 4$, $\sigma_k = 1$, $\sigma_\varepsilon = 1.3$, $\sigma_\gamma = 1$ and $\sigma_P = 1$. These values were applied in all the computations discussed below, although a value of $C_{\varepsilon 1} = 1.52$ was used in predicting the case of Becker at al. [16] in order to match the spreading rate of the jet.

2.2. Fluid flow equations closed using Reynolds stress-γ model

Using the same assumptions as made in the previous section, the Reynolds stress-γ turbulence model may be written as:

$$\frac{\partial(\rho\tilde{u})}{\partial z} + \frac{1}{r}\frac{\partial(r\rho\tilde{v})}{\partial r} = 0$$

$$\rho\tilde{u}\frac{\partial\tilde{u}}{\partial z} + \rho\tilde{v}\frac{\partial\tilde{u}}{\partial r} = A_1$$

$$\rho\tilde{u}\frac{\partial\widetilde{u''^2}}{\partial z} + \rho\tilde{v}\frac{\partial\widetilde{u''^2}}{\partial r} = \frac{1}{r}\frac{\partial}{\partial r}\left[rC_S\rho\frac{k}{\varepsilon}\widetilde{v''^2}\frac{\partial\widetilde{u''^2}}{\partial r}\right] + A_{11} \tag{4}$$

$$\rho\tilde{u}\frac{\partial\widetilde{v''^2}}{\partial z} + \rho\tilde{v}\frac{\partial\widetilde{v''^2}}{\partial r} = \frac{1}{r}\frac{\partial}{\partial r}\left[rC_S\rho\frac{k}{\varepsilon}\widetilde{v''^2}\frac{\partial\widetilde{v''^2}}{\partial r}\right] + A_{22}$$

$$\rho\tilde{u}\frac{\partial\widetilde{w''^2}}{\partial z} + \rho\tilde{v}\frac{\partial\widetilde{w''^2}}{\partial r} = \frac{1}{r}\frac{\partial}{\partial r}\left[rC_S\rho\frac{k}{\varepsilon}\widetilde{v''^2}\frac{\partial\widetilde{w''^2}}{\partial r}\right] + A_{33}$$

$$\rho\tilde{u}\frac{\partial\widetilde{u''v''}}{\partial z}+\rho\tilde{v}\frac{\partial\widetilde{u''v''}}{\partial r}=\frac{1}{r}\frac{\partial}{\partial r}\left[rC_S\rho\frac{k}{\varepsilon}\widetilde{v''^2}\frac{\partial\widetilde{u''v''}}{\partial r}\right]+A_{12}$$

$$\rho\tilde{u}\frac{\partial\varepsilon}{\partial z}+\rho\tilde{v}\frac{\partial\varepsilon}{\partial r}=\frac{1}{r}\frac{\partial}{\partial r}\left[rC_\varepsilon\rho\frac{k}{\varepsilon}\widetilde{v''^2}\frac{\partial\varepsilon}{\partial r}\right]+A_\varepsilon$$

$$\rho\tilde{u}\frac{\partial\gamma}{\partial z}+\rho\tilde{v}\frac{\partial\gamma}{\partial r}=\frac{1}{r}\frac{\partial}{\partial r}\left[rC_\gamma\rho\frac{k}{\varepsilon}\left(\widetilde{u''v''}+\widetilde{v''^2}\right)\frac{\partial\gamma}{\partial r}\right]+A_\gamma$$

Here $\widetilde{u''^2}$, $\widetilde{v''^2}$, $\widetilde{w''^2}$ and $\widetilde{u''v''}$ are the four components of the Reynolds stress. Again, due to the thin shear layer approximation, only the *u*-component of the momentum equation is used, and the only component of the mean strain that is considered significant is $\partial\tilde{u}/\partial r$, with the diffusion fluxes significant in directions normal to the predominate flow direction. The assumption of circumferential symmetry also means that $\tilde{w}$ = 0, with $\widetilde{u''w''}$ and $\widetilde{v''w''}$ also zero. The source terms A_1, A_{11}, A_{22}, A_{33}, A_{12}, A_ε and A_γ used in Equation (4) are defined in Table 1.

Table 1: Source terms used in the Reynolds stress-γ model

A_1	$-\frac{1}{r}\frac{\partial\left(r\rho\widetilde{u''v''}\right)}{\partial r}$
A_{11}	$-2\widetilde{u''v''}\,\partial\tilde{u}/\partial r-2/3\rho\varepsilon-C_1\rho\varepsilon\left(\widetilde{u''^2}/k-2/3\right)+\left(C_2+2C_3\right)\rho\widetilde{u''v''}\,\partial\tilde{u}/\partial r$ $+C_{\gamma4}\rho\gamma\left(1-\gamma\right)\varepsilon/k\,\widetilde{u''^2}$
A_{22}	$-2C_S\rho\left(k/\varepsilon\right)\widetilde{w''^2}\left(\left(\widetilde{v''^2}-\widetilde{w''^2}\right)/r^2\right)-2/3\rho\varepsilon-C_1\rho\varepsilon\left(\widetilde{v''^2}/k-2/3\right)$ $-2\left(C_2+C_3\right)\rho\widetilde{u''v''}\,\partial\tilde{u}/\partial r+C_{\gamma4}\rho\widetilde{v''^2}\gamma\left(1-\gamma\right)\varepsilon/k$
A_{33}	$+2C_S\rho\left(k/\varepsilon\right)\widetilde{w''^2}\left(\left(\widetilde{v''^2}-\widetilde{w''^2}\right)/r^2\right)-2/3\rho\varepsilon-C_1\rho\varepsilon\left(\widetilde{w''^2}/k-2/3\right)+C_2\rho\widetilde{u''v''}\,\partial\tilde{u}/\partial r$ $+C_{\gamma4}\rho\widetilde{w''^2}\gamma\left(1-\gamma\right)\varepsilon/k$
A_{12}	$-C_S\rho\left(k/\varepsilon\right)\widetilde{w''^2}\left(\widetilde{u''v''}/r^2\right)-\rho\widetilde{v''^2}\partial\tilde{u}/\partial r-C_1\rho\varepsilon\left(\widetilde{u''v''}/k\right)$ $+\left[C_4k-\left(3/2C_2+C_3\right)\widetilde{u''^2}+C_3\widetilde{v''^2}\right]\rho\,\partial\tilde{u}/\partial r+C_{\gamma4}\rho\widetilde{u''v''}\gamma\left(1-\gamma\right)\varepsilon/k$
A_ε	$-C_{\varepsilon1}\varepsilon/k\,\rho\widetilde{u''v''}\,\partial\tilde{u}/\partial r-C_{\varepsilon2}\rho\varepsilon^2/k+\rho\varepsilon\widetilde{v''^2}\,\partial\gamma/\partial r\,C_{\varepsilon3}/\sqrt{k}$
A_γ	$-\rho C_{\gamma1}\gamma\left(1-\gamma\right)\widetilde{u''v''}/k\,\partial\tilde{u}/\partial r-C_{\gamma2}k^2/\varepsilon\left(\partial\gamma/\partial r\right)^2-C_{\gamma3}\rho\gamma\left(1-\gamma\right)\varepsilon\Gamma/k$

This model is as described in [15] and is based on an extension of the Jones and Musonge [17] second-moment closure, with the Reynolds stress and turbulence energy dissipation rate transport equations modified to incorporate intermittency effects using the approach of Savill [18]. The final term in the source terms of these equations therefore accounts for crossing of the turbulent/non-turbulent interface. The final intermittency equation was derived [15] on the basis of the expression of Dopazo [19], with mass entrainment and bulk convective spatial transport terms based, respectively, on the approaches of Cho and Chung [2] and Byggstoyl and Kollmann [6].

Standard modelling constants [15] were used in conjunction with the model described, with C_1 = 3, C_2 = -0.44, C_3 = 0.46, C_4 = -0.23, C_s = 0.22, C_ε = 0.18, $C_{\varepsilon 1}$ = 1.4, $C_{\varepsilon 2}$ = 1.8, $C_{\varepsilon 3}$ = 0.1, C_γ = 0.16, $C_{\gamma 1}$ = 1.85, $C_{\gamma 2}$ = 0.2, $C_{\gamma 3}$ = 0.16 and $C_{\gamma 4}$ = 0.1. These values were applied in all the computations discussed below, although a modified value of $C_{\varepsilon 1}$ = 1.5 was again used in predicting the case of Becker at al. [16].

2.3. Scalar PDF transport equation

Consider a non-reacting turbulent flow with the PDF equation employed containing only a passive scalar ω, that being the mixture ratio (or mixture fraction). Applying this to Equation (3) for a single species, which means N = 1 and $\omega_\alpha = \omega$ with $<\omega>$ = 1 for pure jet fluid and $<\omega>$ = 0 for pure oxidant, Equation (3) becomes:

$$\frac{1}{\rho} = \frac{\langle \omega \rangle}{\rho_{fuel}} + \frac{(1 - \langle \omega \rangle)}{\rho_{oxy}} \tag{5}$$

From [20] the evolution of the mass weighted probability $P(\vec{r}, \omega; t)$ is given by:

$$\rho \frac{\partial}{\partial t} P + \rho \tilde{v} \frac{\partial P}{\partial r} = -\rho \left(\frac{\partial P}{\partial t} \right)_{turb} + \rho \left(\frac{\partial P}{\partial t} \right)_{mm} \tag{6}$$

Here, $\tilde{v}$ is the mean velocity and σ_p is the Prandtl number for the turbulent diffusion of P. The third and fourth terms in Equation (6) represent turbulent transport in physical space and molecular mixing in compositional space, respectively.

The molecular mixing term in Equation (6) has a number of models available to represent its effect. The simplest is the linear mean square estimation (LMSE) method [20]. If this is modified to take the effect of γ into account, the expression for LMSE mixing becomes:

$$\left(\frac{\partial P}{\partial t} \right)_{mm} = -\frac{\partial}{\partial \omega} \left[\frac{\gamma \varepsilon C_D}{2k} (\omega - < \omega >) P \right] \tag{7}$$

Here, C_D is the ratio of the scalar to mechanical turbulent time scales and ω is the mixture ratio. The justification for implementing γ in Equation (7) in this way arises from the fact that the magnitude of γ has a direct bearing on the molecular mixing term only, and not on the other terms given in Equation (6). Similar reasoning was used by Kollmann and Janicka [4].

The turbulent transport in physical space term in Equation (6) can be approximated using the gradient transport hypothesis. For the k-ε-γ model discussed earlier this term is therefore given as:

$$\left(\frac{\partial P}{\partial t} \right)_{turb} = -\frac{1}{r} \frac{\partial}{\partial r} \left\{ \frac{r \mu}{\sigma_p} \frac{\partial P}{\partial r} \right\} \tag{8}$$

where σ_p is the Prandtl number for scalar transport. In the case of the Reynolds stress-γ model, this term is specified in line with the work of Chen and Kollmann [21] as:

$$\left(\frac{\partial P}{\partial t}\right)_{turb} = -\frac{1}{r}\frac{\partial}{\partial r}\left\{C_S r \rho \widetilde{v''^2}\frac{k}{\varepsilon}\frac{\partial P}{\partial r}\right\} \tag{9}$$

A value of C_D = 4 in Equation (7) was used in all the results discussed below since this was found to give the most accurate predictions in comparisons with experimental data. Pope's [20] considerations indicate that it is not possible for C_D to be universally constant, with the latter work considering variations of this constant between 0.6 and 3.1.

2.4. von Mises coordinates

Equation sets (1) and (4) can be written [14] for parabolic flows in terms of the von Mises coordinates (ψ, z) with:

$$d\psi = \rho\tilde{u} r dr \tag{10}$$

which automatically satisfies mass conservation. Equations (1) then become:

$$\begin{aligned}
\frac{\partial \tilde{u}}{\partial z} &= \frac{\partial}{\partial \psi} r^2 \rho \tilde{u} \mu \frac{\partial \tilde{u}}{\partial \psi} \\
\frac{\partial k}{\partial z} &= \frac{\partial}{\partial \psi} r^2 \rho \tilde{u} \mu \frac{\partial k}{\partial \psi} + \mu \rho \tilde{u} r^2 \left(\frac{\partial \tilde{u}}{\partial \psi}\right)^2 - \frac{\varepsilon}{\tilde{u}} \\
\frac{\partial \varepsilon}{\partial z} &= \frac{\partial}{\partial \psi} r^2 \rho \tilde{u} \mu \frac{\partial \varepsilon}{\partial \psi} + C_{\varepsilon 1} \mu \frac{\varepsilon \rho \tilde{u} r^2}{k}\left(\frac{\partial \tilde{u}}{\partial \psi}\right)^2 - \frac{\varepsilon^2 C_{\varepsilon 2}}{k\tilde{u}} + \frac{\varepsilon^2}{k\tilde{u}} C_{\varepsilon 4}\Gamma \\
\frac{\partial \gamma}{\partial z} &= \frac{\partial}{\partial \psi} r^2 \rho \tilde{u} \mu (1-\gamma)\frac{\partial \gamma}{\partial \psi} + \frac{\rho \tilde{u} r^2 \mu \gamma (1-\gamma) C_{\gamma 1}}{k}\left(\frac{\partial u}{\partial \psi}\right)^2 \\
&\quad + \rho^2 r^2 C_{\gamma 2} \tilde{u} \frac{k^2}{\varepsilon}\left(\frac{\partial \gamma}{\partial \psi}\right)^2 - \rho C_{\gamma 3} \gamma (1-\gamma)\frac{\varepsilon}{k}\Gamma
\end{aligned} \tag{11}$$

The turbulent viscosity μ and Galilean invariance of the scalar Γ must also be redefined as:

$$\begin{aligned}
\mu &= C_\mu \rho \frac{k^2}{\varepsilon}\left[1 + \frac{k^3}{\varepsilon^2} C_{\mu\gamma} \gamma^{-3}(1-\gamma)(\rho\tilde{u} r)^2 \left(\frac{\partial \gamma}{\partial \psi}\right)^2\right] \\
\Gamma &= \frac{k^{5/2}}{\varepsilon^2} \rho \tilde{u} r^2 \left(\frac{\partial \tilde{u}}{\partial \psi}\frac{\partial \gamma}{\partial \psi}\right)
\end{aligned} \tag{12}$$

These equations are simply evolution equations, with ***z*** playing the role of the time-like coordinate.

Applying the von Mises coordinates to the Reynolds stress-γ flow equations similarly gives:

$$
\begin{aligned}
&\frac{\partial \tilde{u}}{\partial z} = \frac{A_1}{\rho \tilde{u}} \\
&\frac{\partial \widetilde{u''^2}}{\partial z} = \frac{\partial}{\partial \psi}\left[C_S r^2 \rho^2 \tilde{u} \frac{k}{\varepsilon} \widetilde{v''^2} \frac{\partial \widetilde{u''^2}}{\partial \psi} \right] + \frac{A_{11}}{\rho \tilde{u}} \\
&\frac{\partial \widetilde{v''^2}}{\partial z} = \frac{\partial}{\partial \psi}\left[C_S r^2 \rho^2 \tilde{u} \frac{k}{\varepsilon} \widetilde{v''^2} \frac{\partial \widetilde{v''^2}}{\partial \psi} \right] + \frac{A_{22}}{\rho \tilde{u}} \\
&\frac{\partial \widetilde{w''^2}}{\partial z} = \frac{\partial}{\partial \psi}\left[C_S r^2 \rho^2 \frac{k}{\varepsilon} \widetilde{v''^2} \frac{\partial \widetilde{w''^2}}{\partial \psi} \right] + \frac{A_{33}}{\rho \tilde{u}} \\
&\frac{\partial \widetilde{u'' v''}}{\partial z} = \frac{\partial}{\partial \psi}\left[C_S \rho^2 r^2 \tilde{u} \frac{k}{\varepsilon} \widetilde{v''^2} \frac{\partial \widetilde{u'' v''}}{\partial r} \right] + \frac{A_{12}}{\rho \tilde{u}} \\
&\frac{\partial \varepsilon}{\partial z} = \frac{\partial}{\partial \psi}\left[C_\varepsilon \rho^2 r^2 \tilde{u} \frac{k}{\varepsilon} \widetilde{v''^2} \frac{\partial \varepsilon}{\partial \psi} \right] + \frac{A_\varepsilon}{\rho \tilde{u}} \\
&\frac{\partial \gamma}{\partial z} = \frac{\partial}{\partial \psi}\left[C_\gamma \rho^2 r^2 \tilde{u} \frac{k}{\varepsilon} \left(\widetilde{u'' v''} + \widetilde{v''^2} \right) \frac{\partial \gamma}{\partial \psi} \right] + \frac{A_\gamma}{\rho \tilde{u}}
\end{aligned}
\tag{13}
$$

Likewise, the PDF transport equation can be written for the *k*-ε-γ and Reynolds stress-γ models, respectively, as:

$$
\begin{aligned}
&\frac{\partial P}{\partial z} = \frac{\partial}{\partial \psi}\left\{ \frac{\mu}{\sigma_P} \rho \tilde{u} r^2 \frac{\partial P}{\partial \psi} \right\} - \frac{1}{\tilde{u}} \frac{\partial}{\partial \omega}\left[\frac{\gamma \varepsilon C_D}{2k} (\omega - < \omega >) P \right] \\
&\frac{\partial P}{\partial z} = \frac{\partial}{\partial \psi}\left\{ \rho^2 \tilde{u} r^2 C_S \widetilde{v''^2} \frac{k}{\varepsilon} \frac{\partial P}{\partial \psi} \right\} - \frac{1}{\tilde{u}} \frac{\partial}{\partial \omega}\left[\frac{\gamma \varepsilon C_D}{2k} (\omega - < \omega >) P \right]
\end{aligned}
\tag{14}
$$

where the last term again represents molecular mixing, and the precise form of the turbulent transport term is dependent of the level of turbulence closure employed.

3. Numerical solution method

3.1. Finite-volume scheme

Equations (11) and (13) contain only diffusive fluxes, while Equation (14) contains both advective (the LMSE molecular mixing term in the PDF equation) and diffusive fluxes. In order to construct a numerical scheme,

physical space is discretised with a mesh spacing $\Delta\psi$, and composition space with mesh spacing $\Delta\omega$. For the fluid variables, mean quantities in a cell at $z = z_n$ are defined by:

$$q_i^{\,n} = \frac{1}{\Delta\psi}\int_{(i-1)\Delta\psi}^{i\Delta\psi} q(\psi, z_n)\, d\psi, \tag{15}$$

where q is one of $(\tilde{u}, k, \varepsilon, \gamma)$. For the PDF a mean value at $z = z_n$ is defined by averaging over both physical and composition space:

$$P^n{}_{ij} = \frac{1}{\Delta\underline{\omega}\Delta\psi}\int_{(i-1)\Delta\psi}^{i\Delta\psi}\int_j P(\omega_1 \cdots \omega_N, \psi, z_n)\, d\underline{\omega}\, d\psi \tag{16}$$

where $\Delta\underline{\omega}$ is the volume of a cell in composition space and $d\underline{\omega} = d\omega_1 \cdots d\omega_N$. The index j refers to the cell in composition space over which the integration is performed.

Given the flow variables at $z = z_n$, their values at $z = z_{n+1}$ can be found from an explicit finite-volume approximation to Equations (11) and (13) of the form:

$$q_i^{\,n+1} = q_i^{\,n} + \frac{\Delta z_n}{\Delta\psi}\left(f_i^{\,r} - f_i^{\,l}\right) + \Delta z_n s_i, \tag{17}$$

where $f_i^{\,l}, f_i^{\,r}$ are approximations to the fluxes at the left/right edges of the ith cell, and s_i is an approximation to the source term. Obviously:

$$f_i^{\,l} = f_{i-1}^{\,r}$$

An approximation that is first-order in Δz is obtained if values at z_n are used to compute the fluxes and source terms. The source terms can be calculated from the mean values in the cell. In order to compute the fluxes, approximations to the flow variables and r at the cell edges are required. The flow variables can be computed from simple averages:

$$q_i^{\,r} = \frac{1}{2}\left(q_{i+1} + q_i\right)\cdot\left(\rho_{i+1} + \rho_i\right) \tag{18}$$

whilst the radius at the cell edges can be obtained using the trapezoidal rule to integrate Equation (10):

$$r_i^{\,r} = \sum_{k=1}^{i} \frac{\Delta\psi}{r_i \rho_i^n \tilde{u}_i^n} \text{ with } r_i = \frac{1}{2}\left(r_i^{\,r} + r_{i-1}^{\,r}\right) \tag{19}$$

This gives a simple recurrence relation for the $r_i^{\,r}$. The flux for a quantity q is then given by:

$$f^r_i = \frac{\left(q^n_{i+1} - q^n_i\right)}{\Delta\psi}\left(r^r_i\right)^2 \rho^r_i \tilde{u}^r_i \mu^r_i, \tag{20}$$

where μ^r_i is calculated from the flow variables at the cell edge. Since this is a central difference approximation to the diffusive terms, the resulting scheme is second-order in $\Delta\psi$.

The procedure for P is similar, except that terms involving gradients in composition space have to be included. Since these are advective, an upwind difference scheme must be used. With the LMSE approximation, the effective advective velocity in the α direction in composition space is:

$$\dot{\omega} = \frac{1}{\tilde{u}}\left(\frac{\gamma\varepsilon C_D}{2k}\left(\omega - \langle\omega\rangle\right)\right) \tag{21}$$

The PDF is then updated via:

$$P^{n+1} = P^n + (\Delta P)_p + \frac{\Delta z}{\Delta\omega}\left[(\dot{\omega}P)^r_i - (\dot{\omega}P)^l_i\right] \tag{22}$$

where $(\Delta P)_p$ is the increment due to the diffusive term in physical space. A first-order upwind approximation is obtained by setting the flux at a cell face perpendicular to the α direction to:

$$\left(\dot{\omega}P\right)^r_i = \begin{cases} \dot{\omega}P^n_l & \text{for } \dot{\omega} > 0 \\ \\ \dot{\omega}P^n_r & \text{for } \dot{\omega} < 0 \end{cases} \tag{23}$$

where P^n_l and P^n_r are the values in the cells on the left and right of the cell face. Here, $\dot{\omega}$ is evaluated at the centre of the cell face.

The numerical scheme presented so far is second-order in Δr, but first-order in Δz and $\Delta\omega$. To achieve second-order accuracy in all variables then involves applying a second-order Godunov scheme [22]. This uses the first-order scheme described to compute an intermediate solution at a half-step, with these values then used to compute the fluxes and source terms for the flow variables which are subsequently used to update them through a complete time-step. The same is done for the flow terms in the PDF equation, although better approximations to the advective fluxes in composition space are required. Further details may be found in [7].

3.2. Adaptive mesh refinement

Unlike most AMR codes, e.g. [9-13], in the present work mesh refinement is on a cell-by-cell basis instead of being organized into patches. This provides a more efficient grid at some increased cost of integration. Considering a thin region in two space dimensions, such as the shear layer of interest in the present work, certain regions will require high resolution. The

scheme employed uses a hierarchy of uniform grids, $G_0 \ldots G_L$, so that if the mesh spacing on G_0 is $(\Delta\psi, \Delta\omega)$, then it is $(\Delta\psi/2^n, \Delta\omega/2^n)$ on G_n. Grids G_0 and G_1 cover the whole computational domain, but finer grids needs only exist in regions that require high resolution. The grid hierarchy is used to generate an estimate of the relative error by comparing solutions on grids with different mesh spacing, and the grid then refines if this error exceeds a defined tolerance E_r, and de-refines if it is less than a second tolerance, E_d. Refinement also occurs in *z*, so that if the step on G_0 is *Δz*, then it is *Δz/2*^{n} on G_n. The integration algorithm is recursive and is described in detail in [7] for integration of grid G_n over time step *Δt*. In the approach used the integration procedure is identical to that of a time-like downstream step Δ*z*.

The simplest way to apply AMR to the system of interest would be to treat it as a problem in *N*+1 dimensions (*r* and the *N* dimensions in composition space). However, this would mean that if a cell is refined in one dimension, then it is also refined in all others. This would not be very efficient since there is no reason why physical and composition space should both be refined at the same place. For example, near the centreline of a jet, there might be very little variation with *r*, but *P* could be very close to a delta-function, which would require a high degree of refinement in composition space. In order to allow different levels of refinement in physical and compositional space, a complete composition space hierarchy is associated with each physical cell on every grid level. The number of levels of refinement of the composition space in a particular physical cell is then determined by the accuracy requirements for that particular cell. So, for example, the maximum number of grid levels will be used in composition space if *P* is close to a delta-function, whereas a smaller number of levels will be used if it is smooth. Further details are given in [7, 8].

4. Results and discussion

In order to validate the modelling strategy described a number of quantitative comparisons have been made with the results of a series of experiments that involved the mixing of a single passive scalar, namely the mixture fraction, in a turbulent round jet. Figures 1 to 7 give comparisons between predictions and the experimental data obtained by Schefer and Dibble [23] in their study of a non-reacting propane jet in a co-flowing air stream. Figure 8 compares predictions with the results obtained by Birch et al [24] who considered a methane jet mixing in still air, while Figures 9 and 10 give results for the propene jet mixing in still argon studied by Dowling and Dimotakis [25]. Finally, Figures 11 and 12 compare predictions with the measurements of Becker et al [16] and Wygnanski and Fielder [26], respectively, who both considered air jets exhausting into quiescent surroundings.

Table 2: Parameters used in computations of the five jets considered

Schefer and Dibble [23]	Levels of adaptation:	4 physical space, 4 compositional space
	Number of coarse cells:	30 physical space, 25 compositional space
	Nozzle diameter	0.0053 m
	Jet fluid density	1.864 kg m^{-3}
	Co-flow density / velocity	1.196 kg m^{-3} / $\tilde{u}$ = 9.2 m s^{-1}
	Initial jet velocity	1/7th power law with $\tilde{u}$ = 69.89 m s^{-1} on centre-line
	Width of computational domain	10 nozzle diameters
Birch et al [24]	Levels of adaptation:	4 physical space, 4 compositional space
	Number of coarse cells:	72 physical space, 25 compositional space
	Nozzle diameter	0.0126 m
	Jet fluid density	0.674 kg m^{-3}
	Ambient density	1.196 kg m^{-3}
	Initial jet velocity	1/7th power law with $\tilde{u}$ = 20.69 m s^{-1} on centre-line
	Width of computational domain	24 nozzle diameters
Dowling and Dimotakis [25]	Levels of adaptation:	4 physical space, 4 compositional space
	Number of coarse cells:	180 physical space, 25 compositional space
	Nozzle diameter	0.0076 m
	Jet fluid density	1.810 kg m^{-3}
	Ambient density	1.662 kg m^{-3}
	Initial jet velocity	1/7th power law with $\tilde{u}$ = 36.24 m s^{-1} on centre-line
	Width of computational domain	60 nozzle diameters
Becker et al [16]	Levels of adaptation:	4 physical space, 4 compositional space
	Number of coarse cells:	72 physical space, 25 compositional space
	Nozzle diameter	0.0064 m
	Jet fluid density	1.196 kg m^{-3}
	Ambient density	1.196 kg m^{-3}
	Initial jet velocity	1/7th power law with $\tilde{u}$ = 159.18 m s^{-1} on centre-line
	Width of computational domain	24 nozzle diameters
Wygnanski and Fielder [26]	Levels of adaptation:	4 physical space, 4 compositional space
	Number of coarse cells:	180 physical space, 25 compositional space
	Nozzle diameter	0.0264 m
	Jet fluid density	1.196 kg m^{-3}
	Ambient density	1.196 kg m^{-3}
	Initial jet velocity	1/7th power law with $\tilde{u}$ = 62.45m s^{-1} on centre-line
	Width of computational domain	30 nozzle diameters

The parameters used in the computations of each of these test cases are given in Table 2, with the numbers of cells and levels of adaption chosen to provide the most computationally economic scheme for numerical convergence in each case, as well as to ensure grid independence of the results. In each case four levels of refinement were used in both physical and compositional spaces. Note that in the figures that follow the scalar mean $\langle\omega\rangle$ is given more conventionally as $\tilde{\omega}$, while the variance is written as $\widetilde{\omega''^2}$.

The work of Schefer and Dibble [23] provides the most complete data set for comparison purposes including, as it does, measurements of the mean and turbulent velocity and scalar fields, as well as intermittency profiles and scalar PDFs at various locations in the flow. Figures 1 and 2 demonstrate reasonable agreement between predictions and observations for the velocity field, and the approximation of constant pressure used in this work appears justifiable in view of these results. Predictions of the mean velocity, and normal and shear stresses, shown in these figures are reasonable, and in line with previous results [15] derived using similar turbulence models coupled to a

prescribed PDF. Clearly, predictions of the Reynolds stress-γ model are superior to those derived on the basis of the eddy viscosity approach, particularly for the normal stresses, although both models under-predict the shear stresses shown in Figure 2. Scalar predictions derived from the coupled physical and compositional space modelling approach using the *k*-*ε*-γ and Reynolds stress-γ models, given in Figures 3 and 4, show similar levels of accuracy when compared to experimental data, with the Reynolds stress-γ model again giving superior performance in terms of predictions of the first and second moments. This is also the case for the intermittency results of Figure 4, with the transition from turbulent to non-turbulent flow predicted accurately by the modified second-moment closure both in terms of the rate of transition and its radial location. These results are again in line with those obtained previously [15]. However, the use of a transported PDF in the present work, rather than the solution of transport equations for the mean mixture fraction and its variance [15], does result in improved predictions of the mixture fraction fluctuations in particular.

Figures 5 and 6 give results for scalar PDF distributions throughout the flow field. Figure 5 gives predictions and data along the jet centre-line where intermittency effects are negligible, with the two approaches employed giving roughly the same distribution for the PDF of the passive scalar at all distances downstream of the source pipe exit. Just beyond the potential core of the jet, at *z/d* = 5.2, the PDF is close to a delta function at ω = 1, although some mixing of the source propane with ambient air has resulted in a tail that extends to lower concentrations. By 10.8 jet diameters downstream the results indicate that the flow is fully turbulent since the PDF distribution has become approximately Gaussian. By 64 diameters the distribution is again tending towards a delta function, indicating that the flow is still turbulent but near to a fully mixed state. Over all the locations considered, predictions obtained on the basis of both turbulence models are comparable and close to observations.

Scalar PDFs at various radial locations and a fixed downstream distance of 30 jet diameters are considered in Figure 6. Predictions derived using the LMSE molecular mixing model and both turbulence modelling approaches are in good qualitative agreement with the experimental data, and reproduce the evolution of the PDF with increasing radial distance from near Gaussian on the jet centre-line, to bi-modal, and ultimately close to a delta function associated with the co-flowing state. The increasing influence of intermittency on the PDF with radial distance is therefore replicated by the predictions, with results derived on the basis of the Reynolds stress-γ model generally in better agreement with the data. The direct influence of intermittency on these predictions is considered in Figure 7, which compares results derived on the basis of the standard Reynolds stress model, and the same model with intermittency effects included. It can be seen that the effect of the intermittency is not only responsible for improved predictions on the jet centre-line, but also for the bimodal distributions associated with its increasing influence with radial distance. Apart from on the centre-line, the implementation of γ in the LMSE molecular mixing model, as seen in Equation (8), is the primary influence in this respect, with the effect of γ in the flow Equations (11) and (13) a secondary effect. All the present results given in Figure 6 are also superior to those obtained in earlier work [15] which used

the three-part, prescribed PDF approach of Effelsberg and Peters [27] and which failed to predict the bimodal distributions observed experimentally.

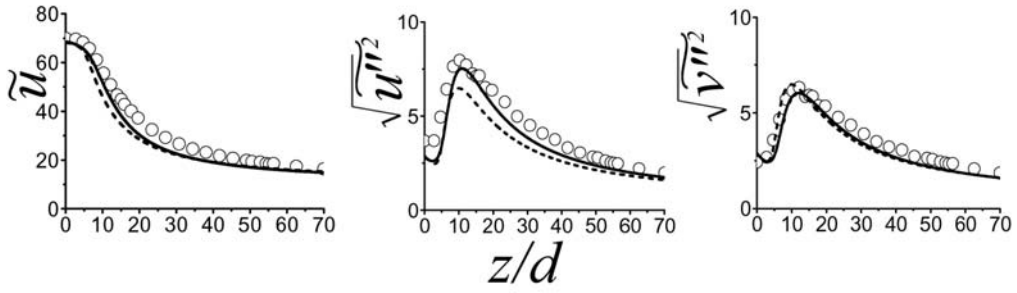

Figure 1: Comparison of measured and predicted axial mean velocity and r.m.s. of normal stresses along the centre-line of the jet (symbols – experimental data [23], solid line – *Re stress-*γ predictions, dash line – *k-*ε*-*γ predictions).

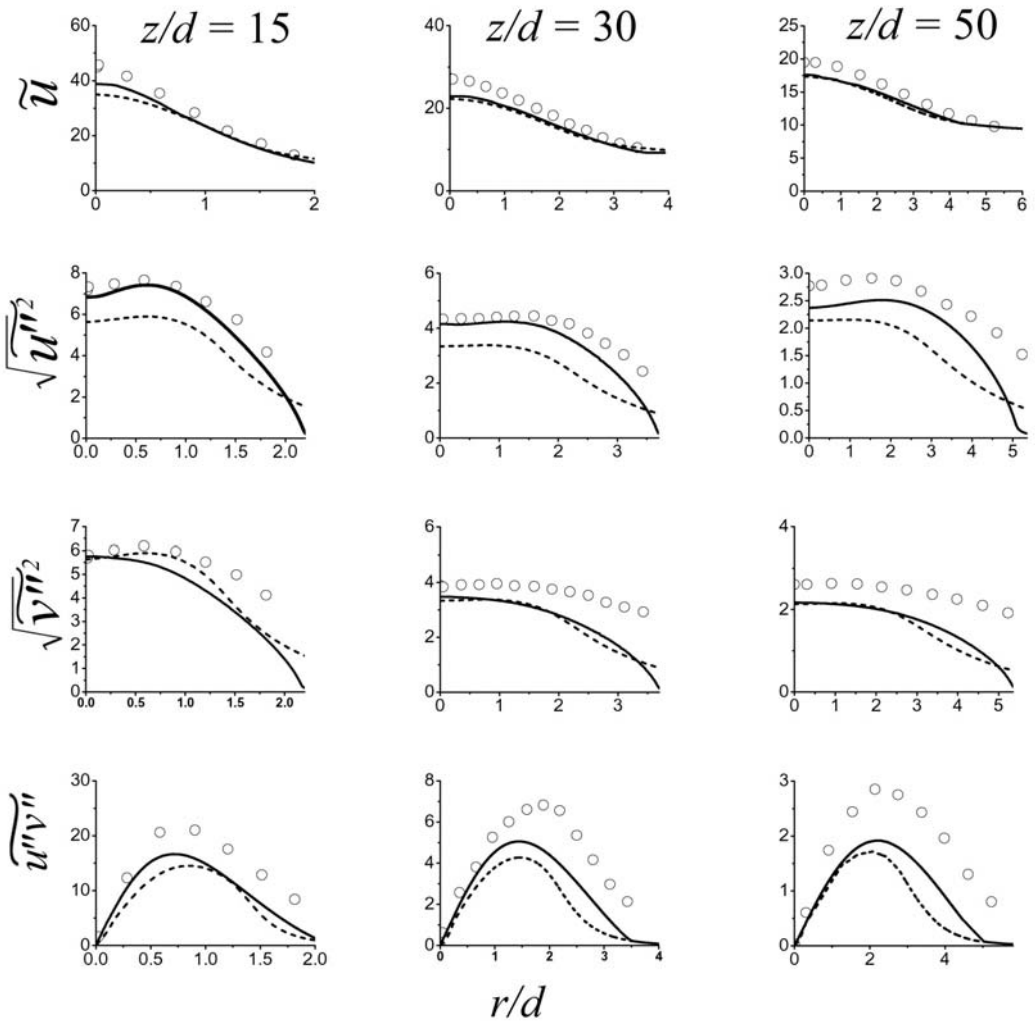

Figure 2: Comparison of measured and predicted radial distributions of axial mean velocity, and r.m.s. of normal stresses and shear stress, at various axial locations (symbols – experimental data [23], solid line – *Re stress-*γ predictions, dash line – *k-*ε*-*γ predictions).

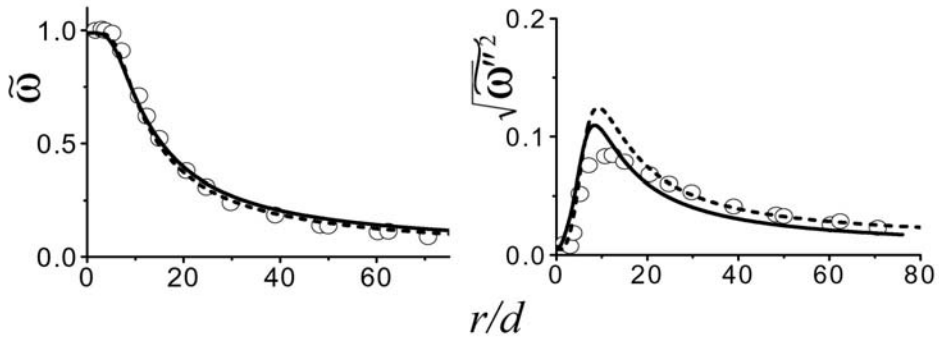

Figure 3: Comparison of measured and predicted mean mixture fraction and r.m.s. of mixture fraction fluctuations along the centre-line of the jet (symbols – experimental data [23], solid line – *Re stress-*γ predictions, dash line – *k-*ε*-*γ predictions).

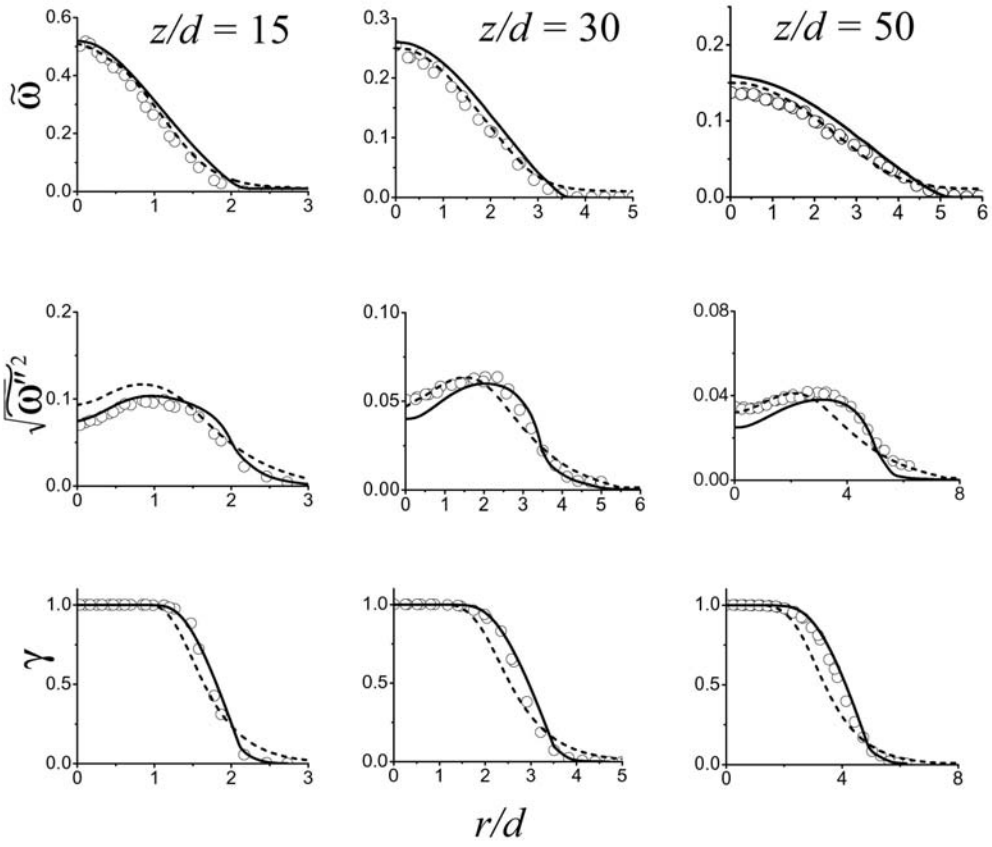

Figure 4: Comparison of measured and predicted radial distributions of mean mixture fraction, r.m.s. of mixture fraction fluctuations and intermittency at various axial locations (symbols – experimental data [23], solid line – *Re stress-*γ predictions, dash line – *k-*ε*-*γ predictions).

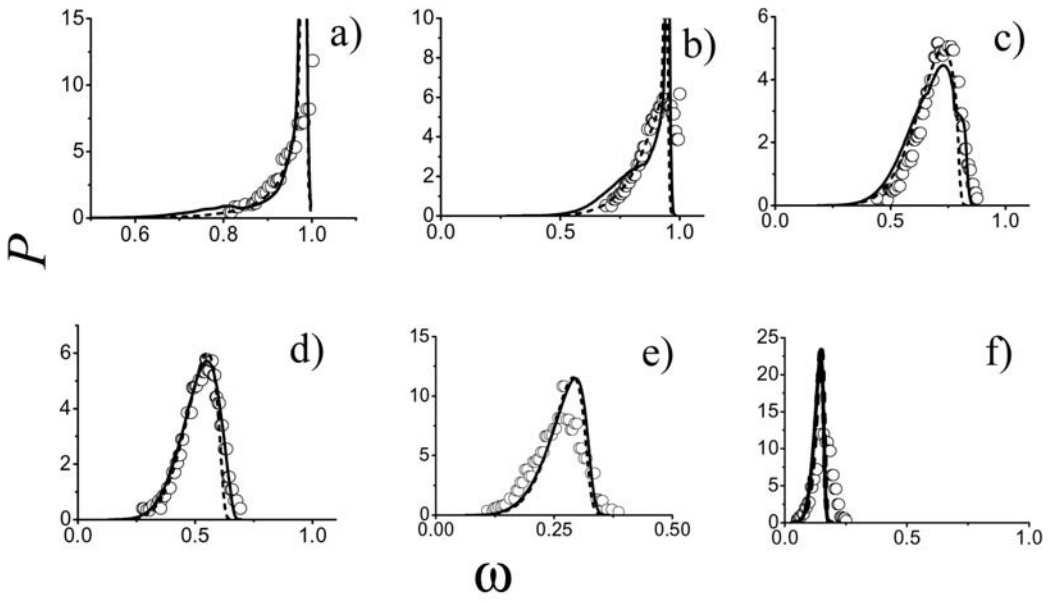

Figure 5: Comparison of measured and predicted distributions of scalar PDF at various locations along the jet centre-line: (a) *z/d* = 5.2, (b) *z/d* = 7.1, (c) *z/d* = 10.8, (d) *z/d* = 15.0, (e) *z/d* = 30.0 and (f) *z/d* = 64.0 (symbols – experimental data [23], solid line – *Re stress-γ* predictions, dash line – *k-ε-γ* predictions).

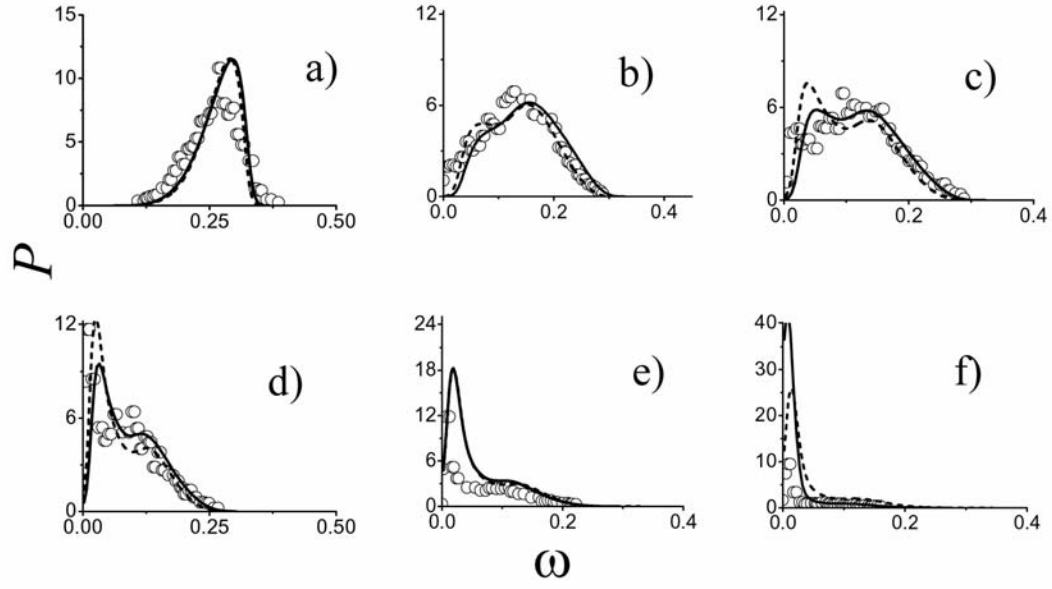

Figure 6: Comparison of measured and predicted distributions of scalar PDF at *z/d* = 30 and various radial locations: (a) *r/d* = 0, (b) *r/d* = 2.0, (c) *r/d* = 2.3, (d) *r/d* = 2.6, (e) *r/d* = 2.9 and (f) *r/d* = 3.2 (symbols – experimental data [23], solid line – *Re stress-γ* predictions, dash line – *k-ε-γ* predictions).

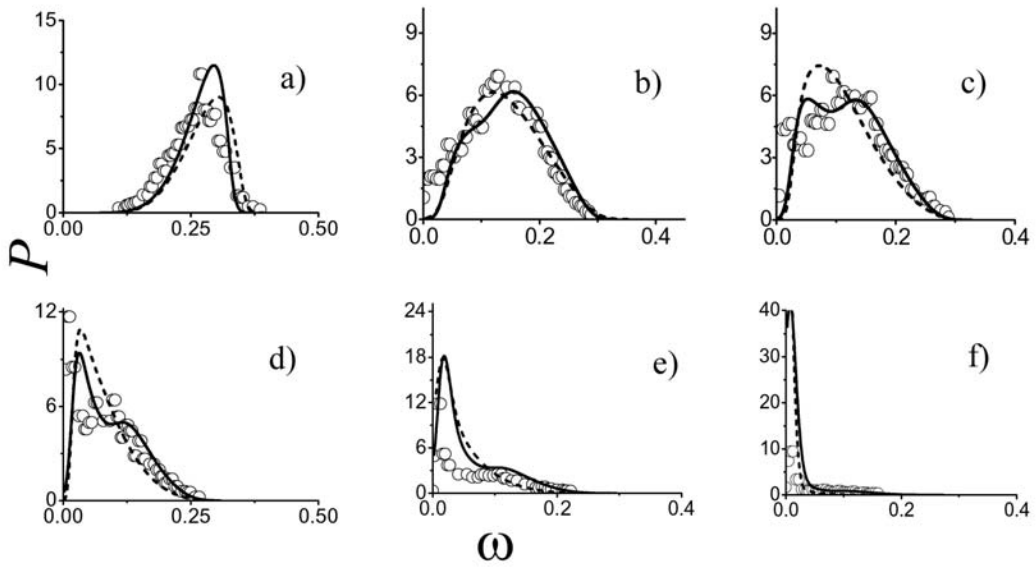

Figure 7: Comparison of measured and predicted distributions of scalar PDF at *z/d* = 30 and various radial locations: (a) *r/d* = 0, (b) *r/d* = 2.0, (c) *r/d* = 2.3, (d) *r/d* = 2.6, (e) *r/d* = 2.9 and (f) *r/d* = 3.2 (symbols – experimental data [23], solid line – *Re stress-*γ predictions, dash line –*Re stress* predictions).

Figures 8 to 10 give further comparisons between predictions of scalar PDFs and data obtained in other studies of jets of lighter [24] and denser [25] than air gases, whilst Figures 11 and 12 similarly compare predictions with alternative [16, 26] measurements of intermittency in air jets.

Figure 8 shows results for the methane jet studied by Birch et al [24]. In this case the predictive approaches described are able to capture the close to Gaussian behaviour on the jet centre-line, and the near delta function distribution at large radial distances, but are less successful in predicting the bimodal distributions observed both at the outer edge of the jet and at lesser radial distances. This contrasts to the results of [15] which show marginally better agreement with data at *r/d* = 1.5 and 1.8, albeit without prediction of the bimodal shape. Comparisons with the data of Dowling and Dimotakis [25], given in Figures 9 and 10 at two downstream locations, are more successful. At *z/d* =30 (Figure 9), the qualitative distribution of the PDFs is successfully predicted, although there is some over-estimation of the magnitude of the PDFs at the two outer radial locations. Similar agreement with data is obtained at *z/d* = 90 (Figure 10), with the over-prediction of the PDF at the outer radial station indicating, as for the results in the previous figure, an over-estimation in the calculations of the rate of mixing with radial distance. As for the majority of previous results, predictions based on the Reynolds stress-γ model are generally in closer accord with these data.

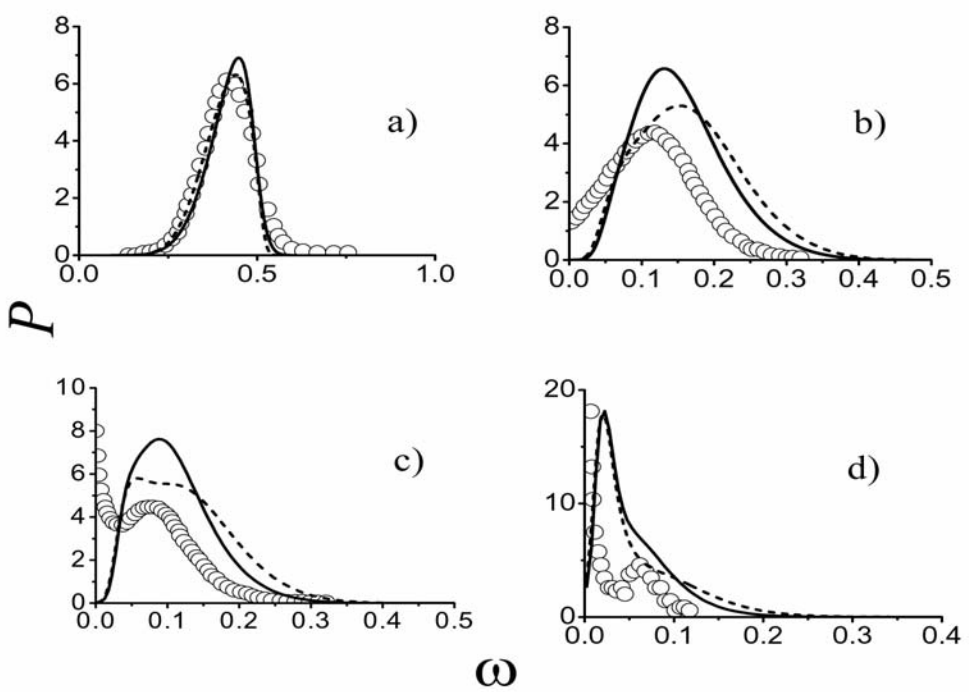

Figure 8: Comparison of measured and predicted distributions of scalar PDF at *z/d* = 10 and various radial locations: (a) *r/d* = 0, (b) *r/d* = 1.3, (c) *r/d* = 1.5 and (d) *r/d* = 1.8 (symbols – experimental data [24], solid line – *Re stress-*γ predictions, dash line – *k-*ε*-*γ predictions).

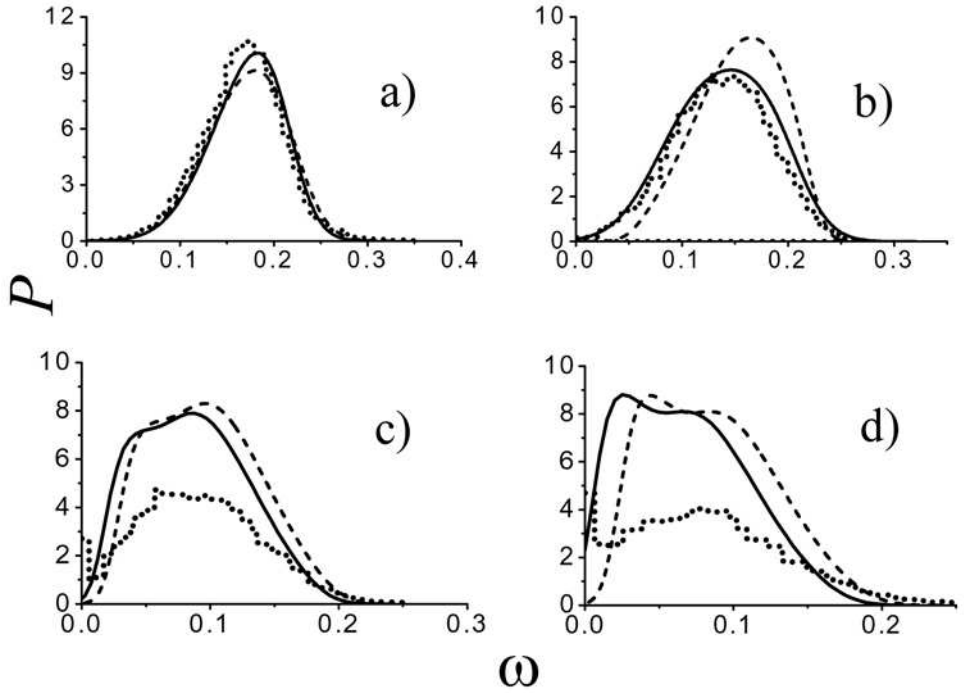

Figure 9: Comparison of measured and predicted distributions of scalar PDF at *z/d* = 30 and various radial locations: (a) *r/d* = 0, (b) *r/d* = 1.77, (c) *r/d* = 3.24 and (d) *r/d* = 3.54 (symbols – experimental data [25], solid line – *Re stress-*γ predictions, dash line – *k-*ε*-*γ predictions).

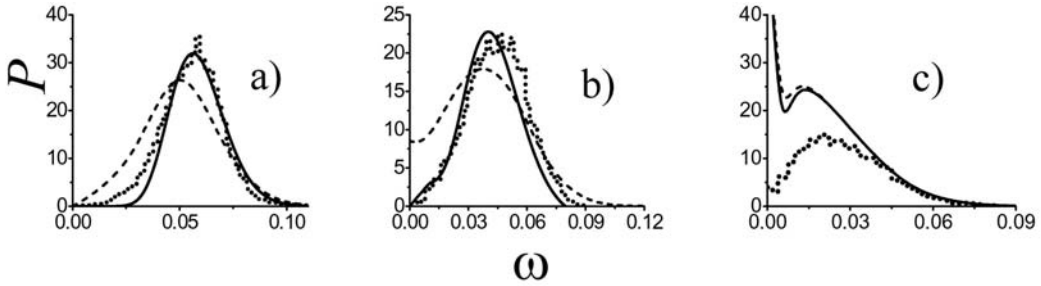

Figure 10: Comparison of measured and predicted distributions of scalar PDF at *z/d* = 90 and various radial locations: (a) *r/d* = 0, (b) *r/d* = 5.37 and (c) *r/d* = 10.74 (symbols – experimental data [25], solid line – *Re stress-*γ predictions, dash line – *k-ε-*γ predictions).

This is also the case for the intermittency profiles given in Figures 11 and 12, with predictions based on the Reynolds stress-γ model again showing better agreement with the data of Becker et al [16] in Figure 11, and that of Wygnanski and Fielder [26] in Figure 12. As for the comparisons with the data of Schefer and Dibble [23], predictions of the latter model again accurately predict the rate of transition from turbulent to non-turbulent flow, as well as its spatial location (apart from at *z/d* = 40 in Figure 12). In contrast, results based on the *k-ε-*γ approach, although in good agreement with the data of Becker et al [16], again tend to under-estimate the rate of the transition in the Wygnanski and Fielder [26] jet, as was also the case for the Schefer and Dibble [23] jet, with a noticeable tail in the predictions at large *r/d* values. These findings are again in line with those of earlier work [15], where similar trends were noted for the Schefer and Dibble [23] and Wygnanski and Fielder [26] jets, although use of a transported PDF in the present work results in the more accurate prediction of intermittency profiles, by the Reynolds stress-γ based approach at least.

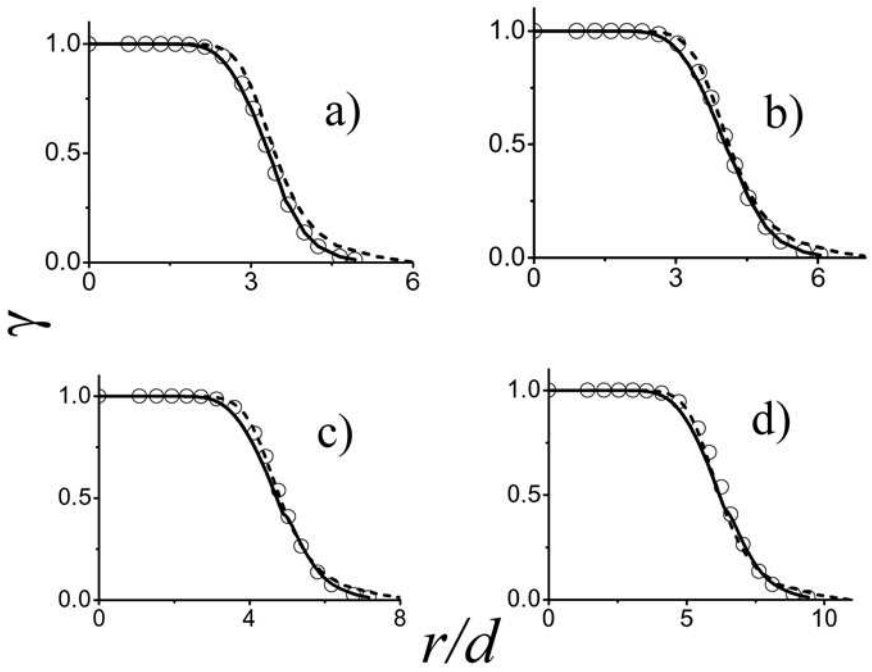

Figure 11: Comparison of measured and predicted radial distributions of intermittency at various axial locations: (a) *z/d* = 20, (b) *z/d* = 24, (c) *z/d* = 32 and (d) *z/d* = 36 (symbols – experimental data [16], solid line – *Re stress-*γ predictions, dash line – *k-ε-*γ predictions).

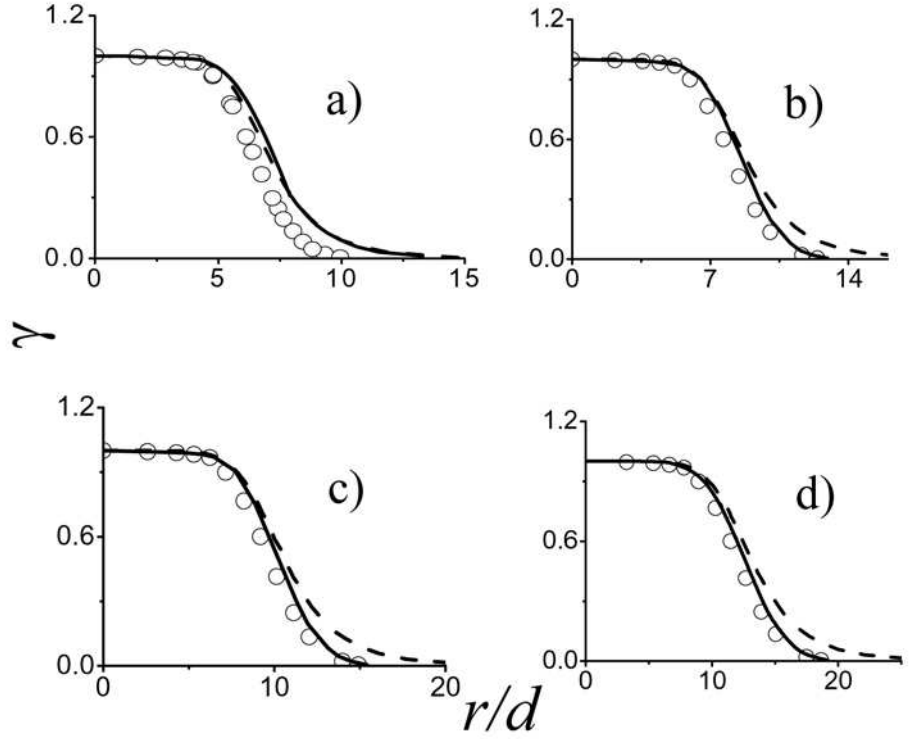

Figure 12: Comparison of measured and predicted radial distributions of intermittency at various axial locations: (a) *z/d* = 40, (b) *z/d* = 50, (c) *z/d* = 60 and (d) *z/d* = 75 (symbols – experimental data [26], solid line – *Re stress-*γ predictions, dash line – *k-ε-*γ predictions).

5. Conclusions

A novel approach for solution of the RANS-based fluid flow equations together with the transported PDF equation for scalar variables has been described, based on the use of a finite-volume method coupled to an adaptive mesh refinement algorithm applied in both physical and compositional space. This method contrasts with conventional approaches to solving the transported PDF equation which generally employ Monte Carlo techniques. The overall model has been applied to the prediction of external intermittency, and its effects, in turbulent round jets using *k-ε-*γ and Reynolds stress-γ turbulence models, with the influence of intermittency also accommodated within the transported PDF equation through modifications to the molecular mixing model employed.

Comparisons with data on the velocity and scalar fields in a number of jets, as well as with measurements of scalar PDFs and intermittency profiles, have demonstrated the ability of the approach described to provide good accuracy in the modelling of intermittent turbulent flows. In particular, and in contrast to earlier approaches [15] which used solutions of transport equations for the mean mixture fraction and its variance to provide predictions of the mixing field, coupled to a prescribed PDF, the present approach is able to provide realistic predictions of the bimodal features to the measured PDFs. Reasonable agreement with measured PDFs and intermittency profiles within the jets examined is also obtained, with results based on the Reynolds stress-γ turbulence model generally in closer accord with experimental data.

Acknowledgements

The authors wish to thank the Engineering and Physical Sciences Research Council for their financial support of the work reported in this paper under EPSRC grant EP/E03005X/1.

References

[1] Pope SB. An explanation of the turbulent round-jet/plane-jet anomaly. AIAA J 1978;3:279-281.
[2] Cho JR, Chung MK. A k-ε-γ equation turbulence model. J Fluid Mech 1992; 237:301-322.
[3] Byggstoyl S, Kollmann W. Closure model for intermittent turbulent flows. Int J Heat Mass Transfer 1981;24:1811-1822.
[4] Kollmann W, Janicka J. The probability density function of a passive scalar in turbulent shear flows. Phys Fluids 1982; 25:1755-1769.
[5] Janicka J, Kollmann W. Reynolds-stress closure model for conditional variables. In: Bradbury LJS, Durst F, Launder BE, Schmidt FW, Whitelay JH, editors. Turbulent shear flows 4. Springer; 1983. p. 73-86.
[6] Byggstoyl S, Kollmann W. A closure model for conditional stress equations and its application to turbulent shear flows. Phys Fluids 1986; 29:1430-1440.
[7] Olivieri DA, Fairweather M, Falle SAEG. An adaptive mesh refinement method for solution of the transported PDF equation. Int J Numer Meth Eng 2009;79:1536-1556.
[8] Olivieri DA, Fairweather M, Falle SAEG. Adaptive mesh refinement applied to the scalar transported PDF equation in a turbulent jet. Int J Numer Meth Eng, in press.
[9] Berger MJ, Oliger J. Adaptive mesh refinement for hyperbolic partial differential equations. J Comp Phys 1984;53:484-512.
[10] Berger MJ, Colella P. Local adaptive mesh refinement for shock hydrodynamics. J Comp Phys 1989;82:64-84.
[11] Bell J, Berger M, Saltzmann J, Welcome M. Three dimensional adaptive mesh refinement for hyperbolic conservation laws. SIAM J Sci Comput 1994;15:127-138.
[12] Quirk JJ. A parallel adaptive grid algorithm for computational shock hydrodynamics. Appl Numer Math 1996;20:427-453.
[13] Baum JD, Lohner R. Numerical simulation of shock-elevated box interaction using an adaptive finite shock capturing scheme. AIAA 1989; AIAA-1989-653.
[14] Spalding DB. GENMIX: A general computer program for two dimensional parabolic phenomena. Oxford: Pergamon Press; 1977.
[15] Alvani RF, Fairweather M. Prediction of the ignition characteristics of flammable jets using intermittency-based turbulence models and a prescribed pdf approach. Comput Chem Eng 2008;32:371-381.
[16] Becker HA, Hottel HC, Williams GC. The nozzle fluid concentration field of the round turbulent, free jet. J Fluid Mech 1967;30:285-303.
[17] Jones WP, Musonge P. Closure of the Reynolds stress and scalar flux equations. Phys Fluids 1988;31:3589-3604.

[18] Savill AM. New strategies in modelling by-pass transition. In Launder BE, Sandham ND, editors. Closure strategies for turbulent and transitional flows. Cambridge University Press; 2002. p. 493-521.
[19] Dopazo C. On conditioned averages for intermittent turbulent flows. J Fluid Mech 1977;81:433-438.
[20] Pope SB. PDF methods for turbulent reactive flows. Prog Energ Combust 1985;11:119-192.
[21] Chen JY, Kollmann W. Pdf modelling of chemical non-equilibrium effects in turbulent non-premixed hydrocarbon flames. Proc Combust Inst 1988;22:645-653.
[22] Godunov SK. Finite difference methods for numerical computations of discontinuous solutions of the equations of fluid dynamics. Mat Sb 1959;47:271-306.
[23] Schefer RW, Dibble RW. Mixture fraction field in a turbulent non-reacting propane jet. AIAA J 2001;39:64-72.
[24] Birch AD, Brown DR, Dodson MG, Thomas JR. The turbulent concentration field of a methane jet. J Fluid Mech 1978;88:431-449.
[25] Dowling DR, Dimotakis PE. Similarity of the concentration field of gas-phase turbulent jets. J Fluid Mech 1990;218:109-141.
[26] Wygnanski I, Fielder H. Some measurements in the self-preserving jet. J Fluid Mech 1969;38:577-612.
[27] Effelsberg E, Peters N. A composite model for the conserved scalar PDF. Combust Flame 1983;50:351-360.